Ultrafast opto-magnetic effects in the extreme ultraviolet spectral range

HENNECKE, Martin, VON KORFF SCHMISING, Clemens, YAO, Kelvin, JAL, Emmanuelle, VODUNGBO, Boris, CHARDONNET, Valentin, LÉGARÉ, Katherine, CAPOTONDI, Flavio, NAUMENKO, Denys, PEDERSOLI, Emanuele, LOPEZ-QUINTAS, Ignacio, NIKOLOV, Ivaylo P., RAIMONDI, Lorenzo, DE NINNO, Giovanni, SALEMI, Leandro, RUTA, Sergiu <http://orcid.org/0000-0001-8665-6817>, CHANTRELL, Roy, OSTLER, Thomas, PFAU, Bastian, ENGEL, Dieter, OPPENEER, Peter M., EISEBITT, Stefan and RADU, Ilie

This document is the Supplemental Material

Citation:

Copyright and re-use policy

SUPPLEMENTARY INFORMATION

Ultrafast Opto-magnetic Effects in the Extreme Ultraviolet Spectral Range

Martin Hennecke,[*] Clemens von Korff Schmising, Kelvin Yao, Emmanuelle Jal, Boris Vodungbo,
Valentin Chardonnet, Katherine Légaré, Flavio Capotondi, Denys Naumenko, Emanuele Pedersoli,
Ignacio Lopez-Quintas, Ivaylo P. Nikolov, Lorenzo Raimondi, Giovanni De Ninno, Leandro Salemi,
Sergiu Ruta, Roy Chantrell, Thomas Ostler, Bastian Pfau, Dieter Engel, Peter M. Oppeneer,
Stefan Eisebitt, Ilie Radu[*]

[*]   hennecke@mbi-berlin.de; ilie.radu@xfel.eu

Contents

Supplementary Notes:

Supplementary Note 1: EXPERIMENTAL TECHNIQUES AND DATA ACQUISITION

The time-resolved pump-probe measurements shown in the main article were carried out at the DiProI end-station using the FEL-1 beamline of the seeded free-electron laser (FEL) FERMI[1], employing the magneto-optical Faraday and Kerr effect to measure the time evolution of the GdFeCo sample magnetization as a function of XUV excitation photon energy, polarization and fluence. The magnetization dynamics of the sample were probed under an incidence angle of 45°, employing linearly polarized, ≈90 fs (FWHM), 400 nm optical pulses generated by a frequency-doubled Ti:sapphire laser system. Since the laser system shares an oscillator with a similar Ti:sapphire laser that provides the seeding pulses for initiating the FEL lasing process, the XUV pump and optical probe pulses are intrinsically synchronized and the jitter between the two pulses is reduced to ≈10 fs (see Ref. 2). Both Faraday and Kerr rotation of the polarization axis of the probing pulses were measured simultaneously in transmission and reflection geometry, respectively, by two independent polarization-sensitive detection setups using Wollaston prisms and balanced photo diodes. An electromagnet applying a saturating magnetic field of ±8 mT perpendicular to the sample plane was used to restore the initial magnetization state of the sample after each pump-probe cycle. Additionally, the magnetic field was flipped every 200 pulses to obtain a magnetic contrast corresponding to the difference between the Faraday and Kerr signals measured for opposite magnetic field directions. The delay between pump and probe pulses was adjusted via an optical delay stage in the probe beam path. Both the FEL and the optical laser system were running at a repetition rate of 50 Hz. By seeding only every second accelerated electron bunch in the modulator section of the FEL, the XUV pump repetition rate is effectively reduced to 25 Hz, allowing for an interleaved measurement of the pumped and unpumped states of the sample. Fast oscilloscopes triggered by the time base of the FEL were used to record and split the pumped and unpumped signals of the balanced photo diodes. The acquired Faraday rotation signals, i.e., the pumped and unpumped state for opposite magnetic field directions as a function of pump-probe delay and XUV polarization, are shown exemplarily in Supplementary Figure 1 for an incident excitation fluence of 4.7 mJ/cm² at a photon energy of 64.0 eV.

In order to excite the sample using different XUV photon energies, the wavelength of the FEL was adjusted by either changing the FEL seeding laser wavelength and the undulators gap between the magnetic sections, or by changing the harmonic order of the emitted radiation. Supplementary Table 1 shows the FEL parameters used in the experiment. A spectrometer in the XUV beam path was used to record the spectrum of the FEL shots in order to determine the spectral bandwidth, i.e., the energy resolution, by fitting the spectrum with a Gaussian function. The FEL pulse durations were determined according to Ref. 3, scaling with the seeding laser pulse length of ≈170 fs and inversely with the harmonic order of the FEL. The resulting pulse lengths show only negligible dependence on the XUV wavelengths used in our experiment and are thus approximated by ≈90 fs. At each photon energy, the polarization of the XUV was alternated between linear horizontal, σ_- and σ_+ by moving the undulator of the FEL. The degree of circular polarization after transmission through the DiProI beamline was characterized in Ref. 4 and shown to be consistently above 90% for both σ_- and σ_+ up to XUV wavelengths of 60 nm, approaching almost ≈100% in the lower wavelength range below 25 nm. Thus, tuning the XUV wavelength in a range from 19.37 to 24.31 nm, any change in helicity due to the different wavelengths is expected to be on the order of ≈1% or less, thus not significantly impacting the polarization state of the XUV pulses. Previous pump-probe studies reported by the authors of Ref. 5, which were carried out at the same end station utilizing a similar wavelength and fluence range, have further demonstrated the very high reproducibility and intensity correlation when switching the helicity of the FEL radiation between σ_- and σ_+. Changing the incident pump fluence on the sample was accomplished by attenuating the FEL pulse energies using solid-state aluminum filters of different thicknesses (100−500 nm) for rough adjustments and a variable pressure inside of a gas absorber for fine-tuning. The resulting attenuation, average pulse energy and shot-to-shot fluctuations of the FEL could be monitored by two I_0 gas monitor detectors (GMD) before and after the attenuator.

For optimizing the pump-probe conditions, the spot sizes (FWHM) of the FEL pump and optical probe pulses were adjusted and measured directly in the sample plane by covering parts of the sample with a layer of fluorescent paint and profiling the beam spots on a camera, leading to an uncertainty of ≈5−10% in FWHM due to this method. The XUV pump spot size was adjusted to 300×300 μm² using a

Kirkpatrick-Baez (KB) mirror focusing system in front of the experimental chamber. The spot size of the probing laser was tuned to 85×85 µm² via optical lenses. The delay between pump and probe pulses was adjusted via an optical delay stage in the probe beam path. For spatial overlap, the probing spot was centered within the much larger pump spot, in order to probe a homogeneously pumped area. Additionally, a YAG screen placed before the KB mirrors was used to validate the XUV beam size and position before the focusing optics. Spot sizes and pump-probe overlap were checked regularly throughout the experiment in order to assure reliable and stable pump-probe conditions and minimize any systematic error that could emerge from temporal drifts or a change of FEL parameters, especially after changing photon energy and polarization.

Supplementary Note 2: DATA SORTING AND DATA TREATMENT

The recorded time-resolved Faraday and Kerr data were sorted by incident excitation fluence using the pulse energies of the FEL shots recorded by the I_0-GMD. Shot-to-shot fluctuations of the FEL source lead to a statistical distribution of pulse energies around an average value targeted by the attenuator settings. Thus, each data set collected during a single pump-probe delay scan contains a large amount of fluence-dependent information that can be extracted.

Supplementary Figure 2 shows exemplary the histograms of FEL pulse energies per shot of three consecutive pump-probe delay scans recorded at different average excitation fluences. Sorting the data by pulse energy using a step size of 1 µJ and averaging only over the Faraday and Kerr probe belonging to the same interval of (x±0.5) µJ allows obtaining a fluence-dependence with a high density of points. The binning window widths, resulting in an uncertainty of the excitation fluence, were chosen as a trade-off between the density of points in the fluence diagram and the signal-to-noise ratio of the averaged Faraday and Kerr signals which is limited by the number of shots that fall into the intervals. Taking also the beamline transmission of ≈60% into account, the pulse energies can be divided by the XUV spot size to obtain the incident fluence in units of mJ/cm² on the sample. Due to the shape of the statistical pulse energy distribution, the data points are generally not equally distributed within each binning window, especially at the rising and falling edges of the distribution (compare the histograms in Supplementary Figure 2). The average fluence of the data points within a binning window is thus not necessarily located at its center. As the fluctuations are random and the shape of the fluence distribution slightly varied between subsequently recorded scans for different polarization and photon energies, the pairs of averaged data points for σ− and σ+ excitation that were subtracted for the determination of ΔM (as shown in Fig. 3 of the main article) possess a slight fluence deviation. The corresponding increased uncertainty of ΔM on the fluence axis is reflected by the error bars, taking into account the fluence mismatch as well as the initial fluence uncertainty via error propagation.

Supplementary Figure 3 shows the full data set of the polarization- and fluence-dependent magnetization dynamics induced by resonant 54.1 eV excitation as a function of pump-probe delay, obtained from sorting the time-resolved magneto-optical Faraday rotation after XUV pump pulse energy. Supplementary Figure 4 shows the corresponding difference between the magnetization transients obtained for σ− and σ+ excitation, i.e., the helicity-dependent effect, as a function of pump-probe delay and excitation fluence. The data shows that especially in the high fluence regime (≥4 mJ/cm²), where the IFE-induced effects are large, the helicity-dependent effect persists until the end of the pump-probe delay range (-2.2 to 30 ps) scanned in the experiment. As discussed in the main article, such long-lived effects on the magnetization are reasonable, as the system needs much longer times compared to the pump pulse duration in order to accommodate the large IFE-induced magnetization changes (up to 30% of equilibrium magnetization). Also for excitation fluences ≥4 mJ/cm² and within the experimental uncertainty, the magnitude of the helicity difference either slowly increases further after the initial sub-picosecond rise or stays constant within this time interval (see, e.g., the data for 4 mJ/cm² and 6 mJ/cm²). This behavior, taking place on a ten picoseconds time scale, can qualitatively be attributed to different recovery times depending on the demagnetization amplitudes after σ− or σ+ excitation, i.e., the magnetization level from which the system has to recover back to the initial state. However, this does not affect the results or conclusions presented in the main article, where the helicity-dependent effect is

quantified based on ΔM values that are obtained from the maximum demagnetization amplitudes at early times (≤ 2 ps), as indicated in the inset of Fig. 2 of the main article.

The data shown in Supplementary Figures 3 and 4 was fitted using a double exponential fit function (solid lines), taking into account the ultrafast demagnetization (Fig. 3) or the helicity-dependent magnetization changes (Fig. 4), the subsequent relaxation process and the experimental time resolution:

$$f(t) = g(t) \otimes \begin{cases} A, & t \leq 0 \\ A - B\left[1 - \exp\left(-\dfrac{t}{\tau_\mathrm{B}}\right)\right] + C\left[1 - \exp\left(-\dfrac{t}{\tau_\mathrm{C}}\right)\right], & t > 0 \end{cases} \tag{1}$$

with A corresponding to the unpumped Faraday signal at negative delays, B and C to the amplitudes of the two exponential components modeling the ultrafast rise or drop and subsequent relaxation processes, and τ_B and τ_C to the respective exponential time constants. By convolution with a Gaussian function $g(t)$, the experimental time resolution of ≈ 280 fs (FWHM) is taken into account, which was determined using the method described in Ref. 6 from the pulse duration of the pump and probe pulses as well as the experimental geometry, i.e., the angle between the two beams and their footprints on the sample.

The obtained exponential time constants of the ultrafast demagnetization process are shown in Supplementary Figure 5a as a function of excitation fluence and XUV polarization. The corresponding time constants of the rising edge of the helicity-dependent effect are shown in Supplementary Figure 5b. The complete set of normalized fit parameters (i.e., with A=1 and A=0, respectively, corresponding to the unpumped state) are provided in Supplementary Tables 2-5. Please note that in the low fluence regime, the limited temporal resolution of the experiment (≈ 280 fs) in conjunction with the low amplitudes of demagnetization and helicity-dependent effect leads to a large uncertainty. It also has to be noted that, apart from the low fluence regime, the scanned pump-probe delay interval does not contain sufficient amount of the recovery dynamics for an accurate fit, which leads to a large uncertainty in the determination of the relaxation amplitudes and time constants.

Supplementary Note 3: FARADAY VS. KERR PROBING

Supplementary Figures 6 and 7 show the maximum demagnetization amplitudes D upon $\sigma_\pm$ and linearly polarized excitation ($D = 1 - \min[M/M_0]$) as well as the differences $\Delta M = D[\sigma_-] - D[\sigma_+]$ as a function of incident excitation fluence for the XUV excitation photon energies of 51.0, 54.1, 56.1 and 64.0 eV, comparing magneto-optical Faraday and Kerr probing. Note that all values are normalized to the equilibrium magnetization in the unexcited state. The data were fitted using sigmoid functions serving as a guide to the eye. The shaded areas in Supplementary Figures 6a and 7a correspond to a 90% confidence interval as an estimation of the experimental uncertainty. The shaded areas in Supplementary Figures 6b and 7b correspond to the different fluence regimes that within the experimental uncertainty indicate the helicity-dependent effect to scale almost linearly with the fluence (white area) until a saturated state is reached where it almost stays constant or starts to decrease again (gray area). The dashed lines serve as a guide to the eye and correspond to linear trends fitted to the different fluence regimes. Comparing the Faraday and Kerr data reveals a slight difference in demagnetization amplitudes, which can be related to the different information depths of the Faraday and Kerr measurements, corresponding either to the whole depth of the sample in transmission or the penetration depth of the optical light in reflection geometry, respectively. Furthermore, the helicity-dependent effect probed by the Kerr rotation undergoes a stronger attenuation in the saturated regime, as the measured demagnetization amplitudes approach the fully demagnetized state for lower excitation fluences compared to the Faraday data.

Supplementary Note 4: COMPARISON TO CIRCULARLY POLARIZED VIS/NIR-PUMPING

In order to *directly* compare the XUV-IFE to the IFE induced by VIS/NIR-pumping of the valence band, additional time-resolved measurements were performed on the very same GdFeCo sample that was used in the XUV-studies presented in the main article. Employing a table-top time-resolved MOKE setup (1.55 eV pump − 3.1 eV probe), the laser-induced demagnetization dynamics were systematically studied as a function of excitation fluence and helicity. The pump pulses were circularly polarized using a $\lambda/4$-wave plate, alternating their helicity between σ_- and σ_+ with ≤0.1% fluence deviation. The results are shown in Supplementary Figure 13, revealing an helicity-dependent effect on the order of ≈1% of the equilibrium magnetization. The magnitude of the effect was obtained in the same way as for the XUV-IFE studies presented in the main article, i.e., from the difference ΔM between the maximum demagnetization amplitudes D induced by the opposite helicities $\sigma_\pm$. These measurements show that the helicity-dependent effects induced by VIS/NIR light are by an order of magnitude smaller compared to the XUV-IFE measured on the same GdFeCo sample, strongly suggesting that the IFE scales indeed with the spin-orbit coupling, which is much stronger for the core-levels than for valence band electrons (e.g., 1.1 eV vs. 65 meV in case of Fe 3p and 3d electrons, respectively[7]).
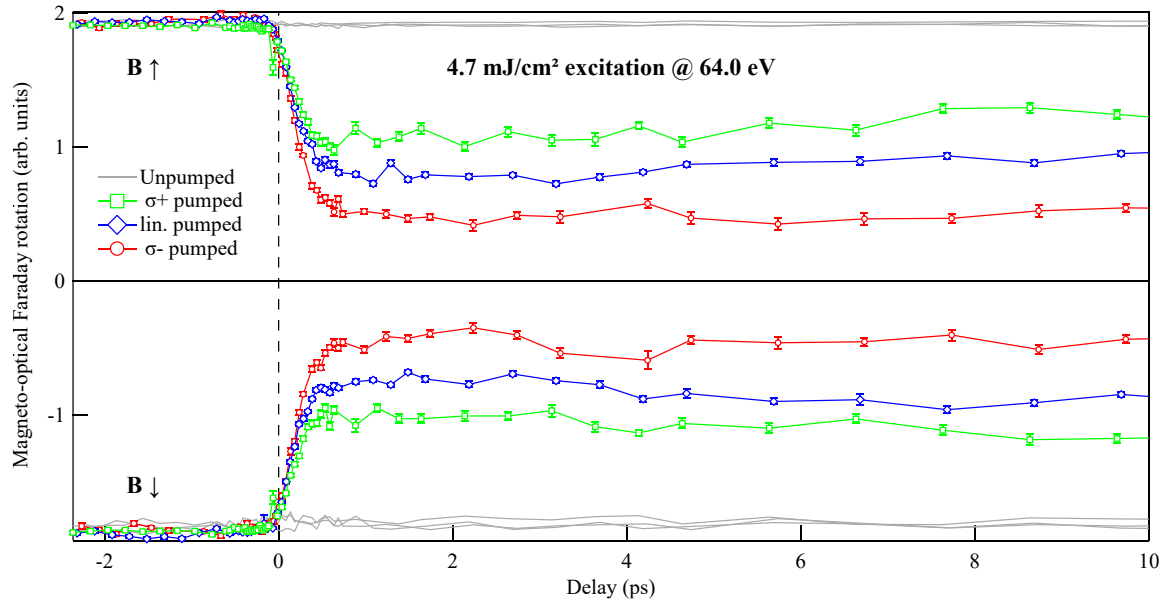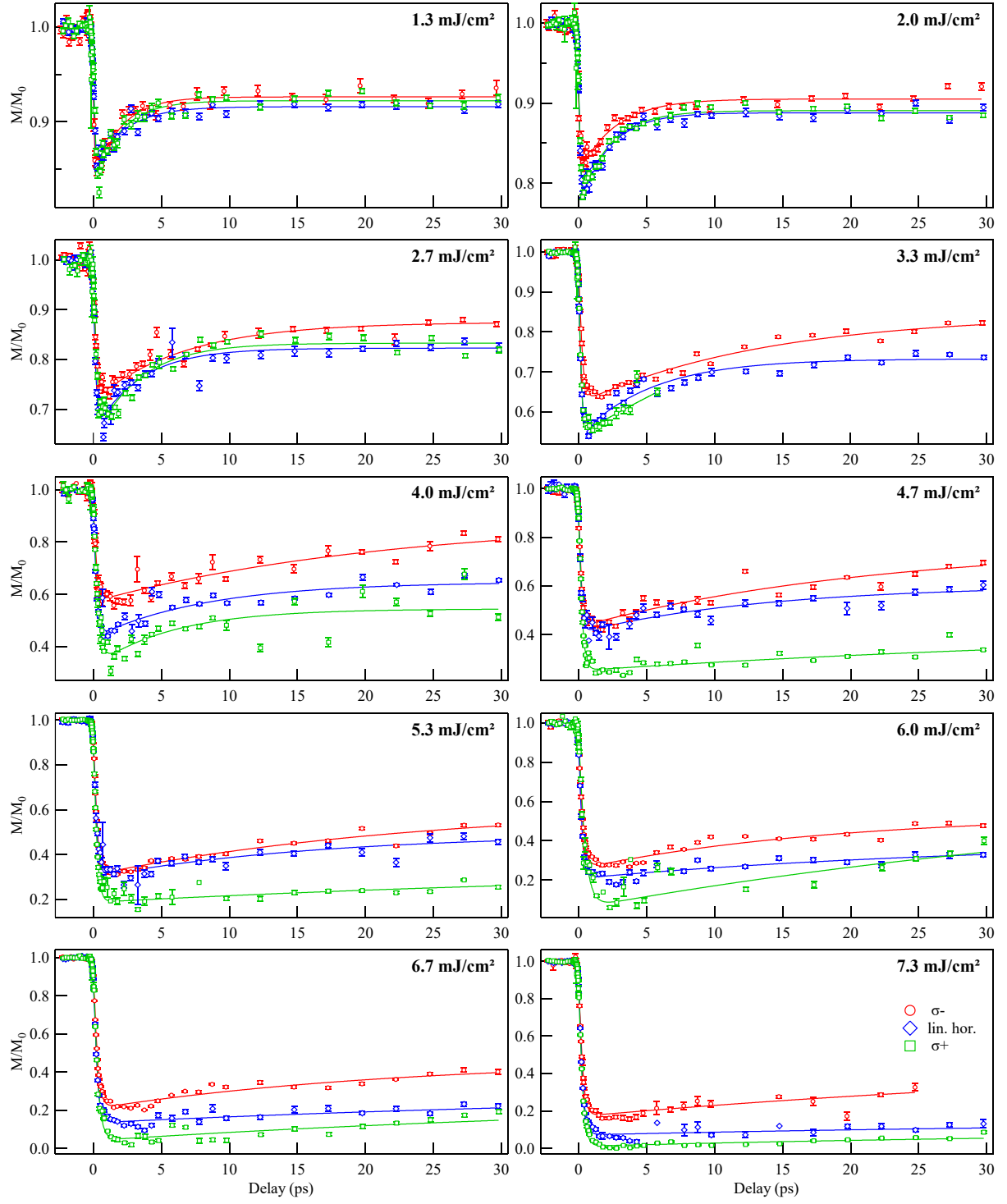
Supplementary Figure 1.
Transient magneto-optical Faraday rotation upon excitation with an incident fluence of 4.7 mJ/cm² and a photon energy of 64.0 eV, recorded for opposite magnetic field (B) directions as a function of pump-probe delay and XUV polarization. The pumped and unpumped states are acquired by probing at 50 Hz repetition rate while pumping at only 25 Hz. The error bars are calculated as the standard error of the mean.
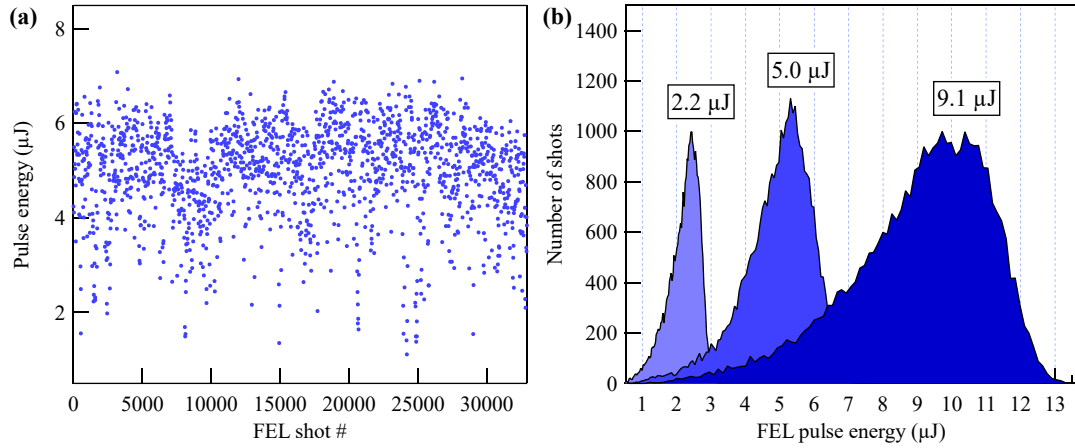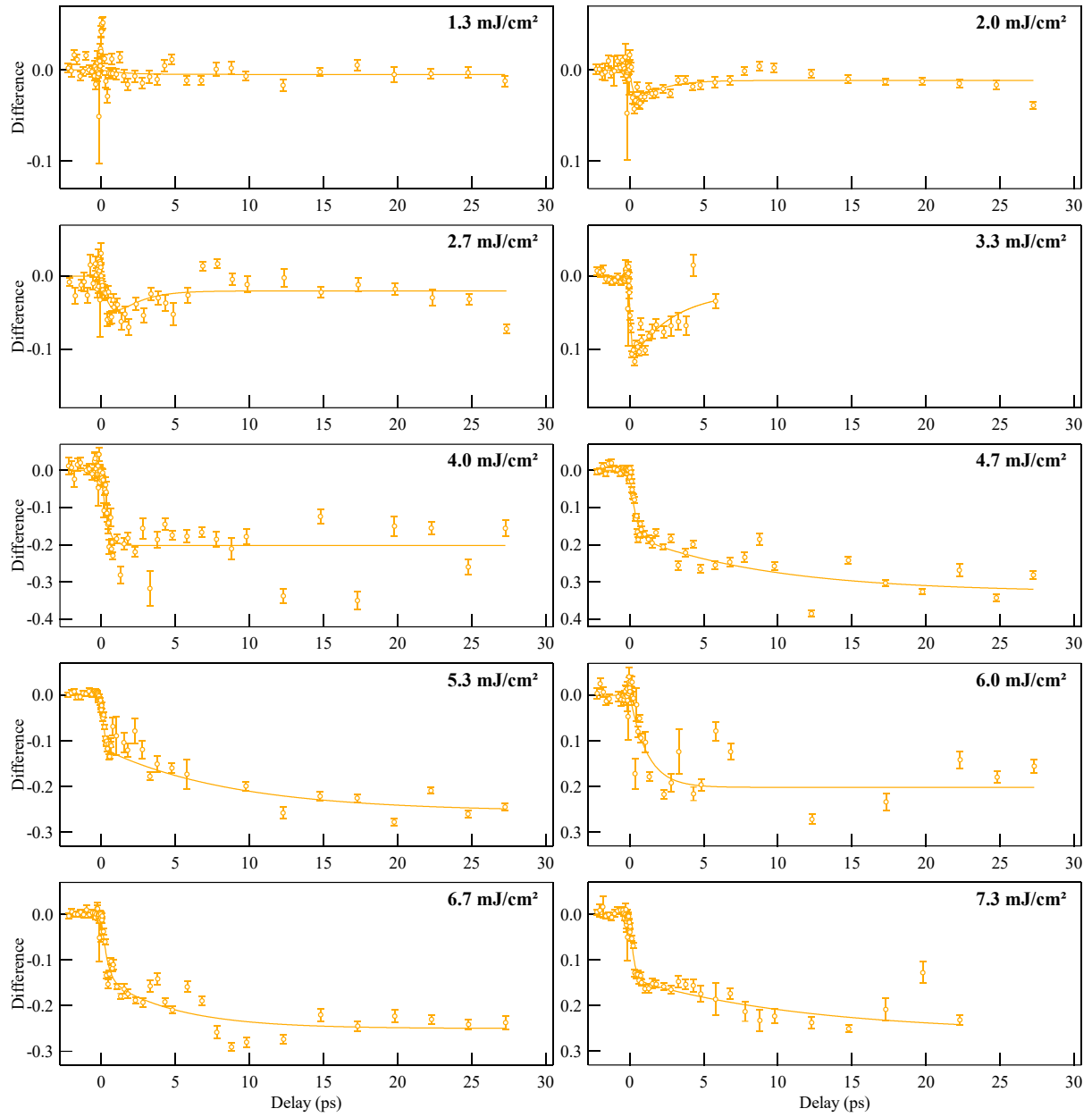

Supplementary Figure 2.
Analysis of the shot-resolved FEL pulse energies recorded by the I_0 gas monitor detector. The graph shows exemplary the data recorded for linearly polarized XUV radiation at a photon energy of 54.1 eV. (**a**) FEL pulse energies per shot as recorded for an average pulse energy of 5.0 µJ. Only every twentieth shot is plotted for better visibility. (**b**) Histograms of the statistical distribution of XUV pulse energies recorded during three subsequent pump-probe delay scans using different average excitation fluences. The Faraday/Kerr data was sorted by averaging only over those data points where the sample was excited by FEL shots with the same pulse energy, as defined by a 1 µJ grid (shown as dashed lines).
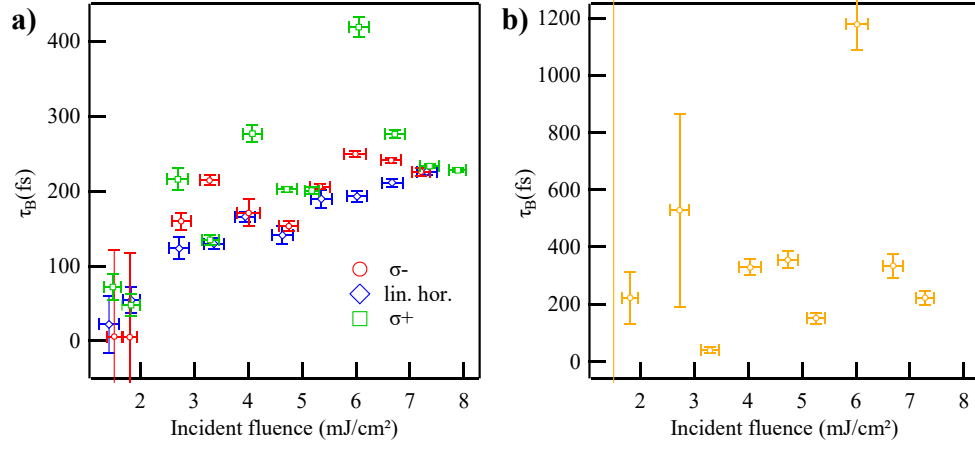
Supplementary Figure 3.
Transient magnetization dynamics of the system induced by XUV pulses of 54.1 eV photon energy, probed by the normalized magneto-optical Faraday rotation as a function of pump-probe delay, XUV polarization and incident excitation fluence. The magnetization is normalized to the equilibrium magnetization in the unexcited state (M/M_0). The error bars are calculated as the standard error of the mean.
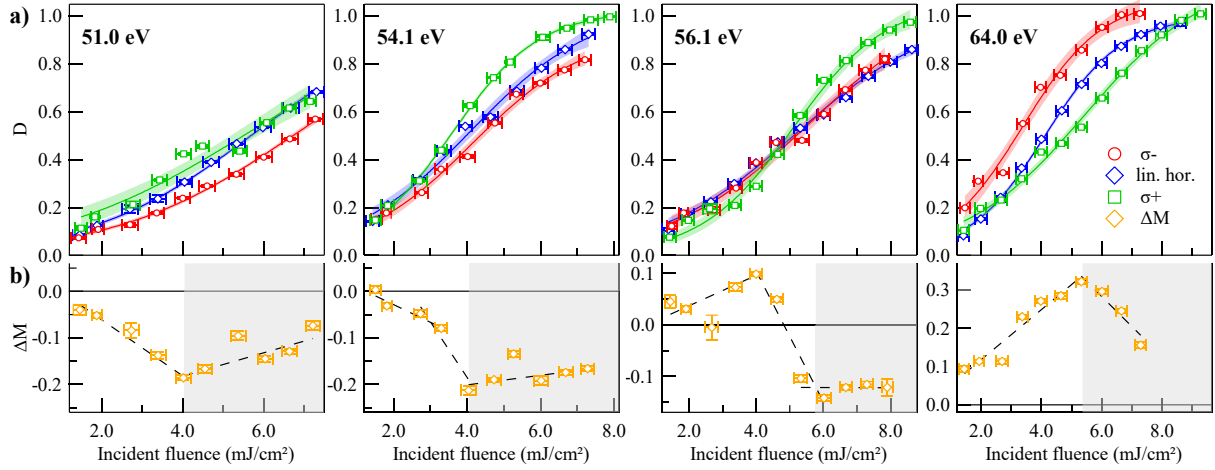
Supplementary Figure 4.
Difference between the magnetization transients obtained for σ₋ and σ₊ excitation (data from Supplementary Figure 3), showing the helicity-dependent effect as a function of pump-probe delay and excitation fluence. The error bars are calculated from the error propagation of the standard error of the mean.

8

Supplementary Figure 5.
Fitted exponential time constants of the data presented in Supplementary Figures 3 and 4 as a function of incident excitation fluence. (**a**) Time constants of the ultrafast demagnetization induced by the three different XUV polarizations. (**b**) Time constants of the rising edge of the helicity-dependent effect. The error bars correspond to the uncertainty of the fitted exponential time constants (y-axis) and the standard error of the mean fluence values obtained by sorting the data after free-electron laser pulse energy (x-axis).
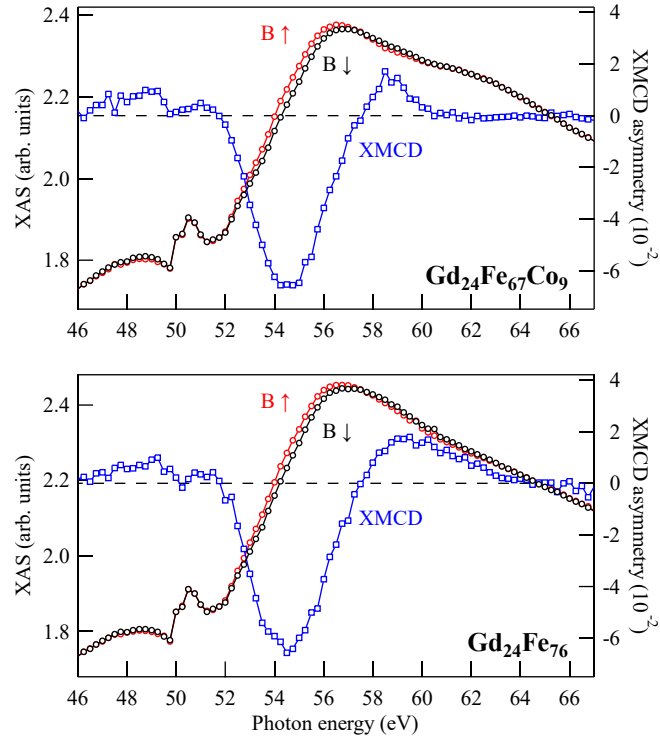
Supplementary Figure 6.
(**a**) Maximum demagnetization amplitudes (*D*) obtained from the transient magneto-optical *Faraday* rotation upon $\sigma_{\pm}$- and linearly polarized excitation (red circles, blue diamonds and green squares), and (**b**) their difference ΔM (yellow diamonds) as a function of incident fluence and XUV photon energy. The error bars of the *D* values correspond to the uncertainty of the fitted demagnetization amplitudes (y-axis) and the standard error of the mean fluence values obtained by sorting the data after the free-electron laser (FEL) pulse energy (x-axis). The error bars of the ΔM values are calculated from the error propagation.
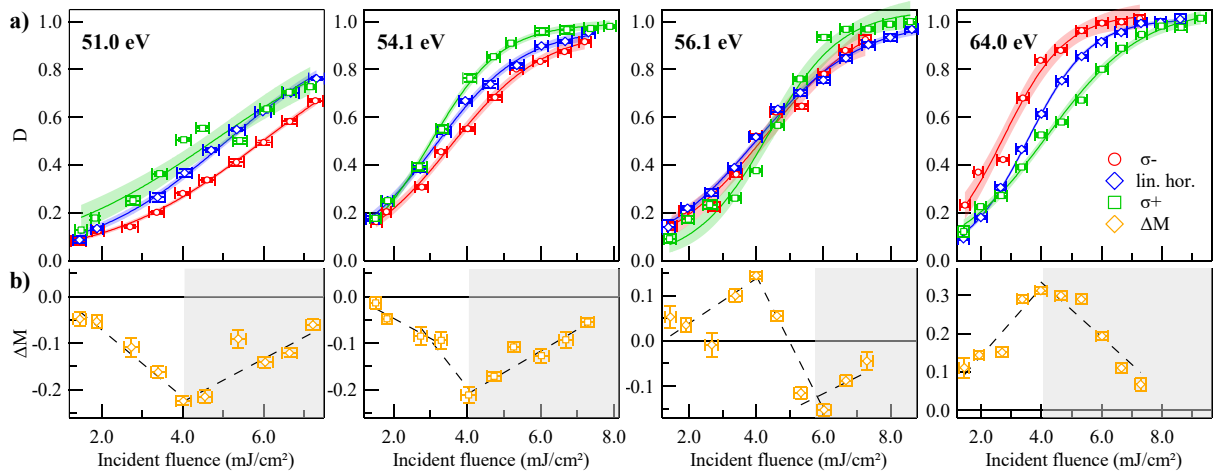
Supplementary Figure 7.
(**a**) Maximum demagnetization amplitudes (*D*) obtained from the transient magneto-optical *Kerr* rotation upon $\sigma_{\pm}$- and linearly polarized excitation (red circles, blue diamonds and green squares), and (**b**) their difference ΔM (yellow diamonds) as a function of incident fluence and XUV photon energy. The error bars of the *D* values correspond to the uncertainty of the fitted demagnetization amplitudes (y-axis) and the standard error of the mean fluence values obtained by sorting the data after the free-electron laser (FEL) pulse energy (x-axis). The error bars of the ΔM values are calculated from the error propagation.

10

Supplementary Figure 8.
Static XUV absorption (XAS, red and black circles, left scale) and XMCD asymmetry spectra (blue squares, right scale) of the $Gd_{24}Fe_{67}Co_9$ and $Gd_{24}Fe_{76}$ samples, measured in the photon energy range of the Fe $M_{3,2}$ resonance. The small peak at 62.0 eV in the XAS of the GdFeCo sample arises due to resonant excitation of the small Co constituent, which is not present in the XAS of the GdFe sample. On the contrary, the XMCD of the GdFeCo sample is suppressed at 62.0 eV compared to GdFe, which can be attributed to the opposite polarity of the Fe and Co XMCD at this photon energy (see, e.g., Ref. 8 for XMCD spectra of elemental Fe and Co), cancelling out each other in their superposition due to the different concentration of Fe and Co in the alloy.
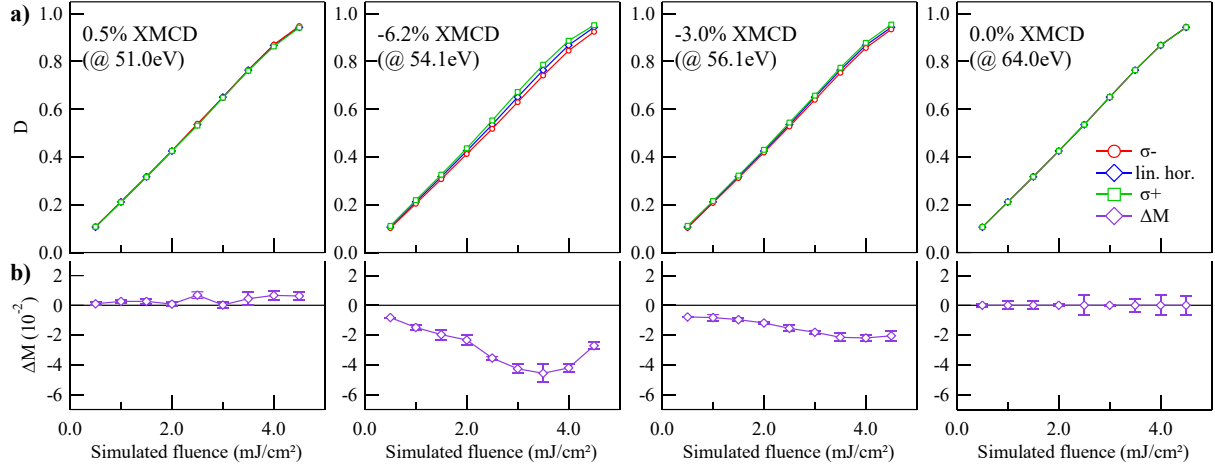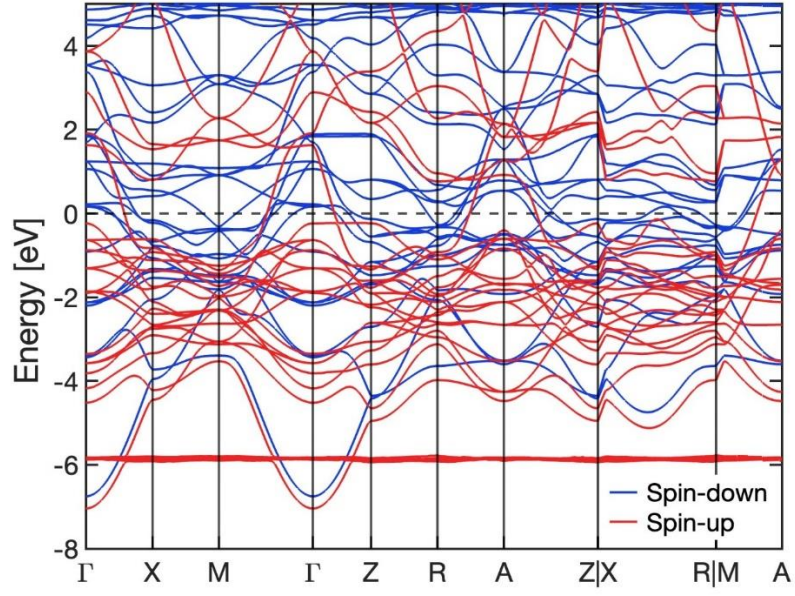
Supplementary Figure 9.
(**a**) Maximum demagnetization amplitudes (D) obtained from ASD simulations for $\sigma_{\pm}$- and linearly polarized excitation (red circles, blue diamonds and green squares) as a function of simulated excitation fluence and magnitude of XMCD, that was set according to the static XMCD spectroscopy of the sample, and (**b**) the corresponding difference ΔM (purple diamonds). The error bars are obtained by varying the input values for the XMCD magnitude by $\pm 0.5\%$.
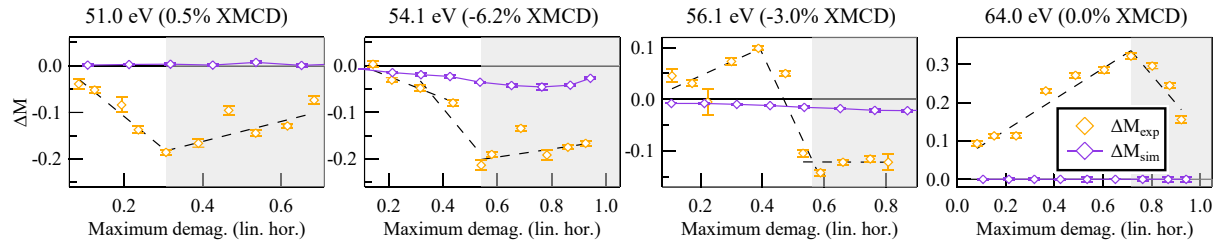
Supplementary Figure 10.
Experimentally observed (yellow color, compare Supplementary Figure 6) and simulated (purple color, compare Supplementary Figure 9) ΔM values as a function of the maximum demagnetization amplitudes induced by linearly polarized excitation of the same fluence. The error bars of ΔM_{sim} are obtained by varying the input values for the XMCD magnitude by $\pm 0.5\%$. The error bars of ΔM_{exp} are calculated from the error propagation of the demagnetization amplitudes shown in Supplementary Figure 6.
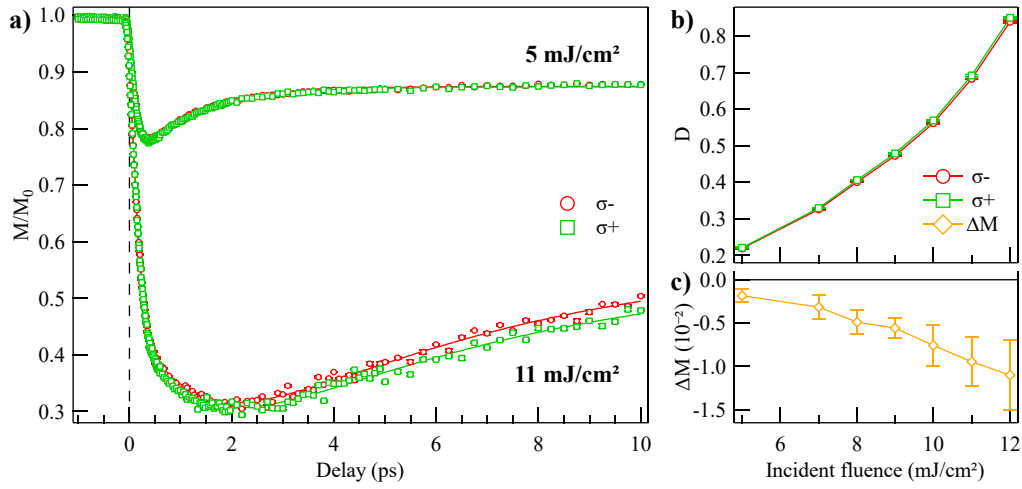
Supplementary Figure 11.
Calculated spin-polarized band structure of $GdFe_2Co$ along high-symmetry lines of the simple tetragonal Brillouin zone, with special symmetry points as indicated.
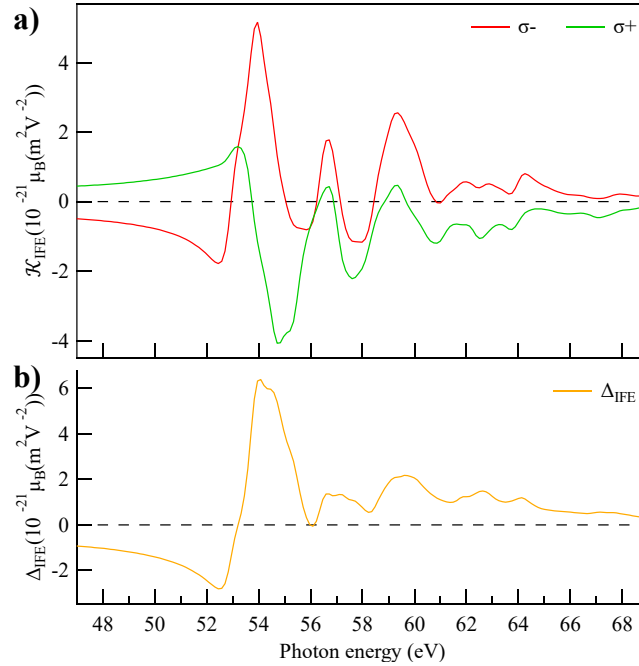
Supplementary Figure 12.
Static *ab initio* calculations of the Inverse Faraday Effect (IFE) constant $\mathcal{K}^{\text{IFE}}$ in the XUV spectral range for a $GdFe_2Co$ unit cell. (**a**) The calculated total opto-magnetic response to $\sigma_{\pm}$-polarized XUV radiation as a function of photon energy, i.e., the sum over the spin (S) and orbital (L) responses to left (σ_-) and right (σ_+) circularly polarized excitation, respectively. (**b**) The corresponding difference Δ_{IFE} between the total opto-magnetic constants, which is also shown in Fig. 4 of the main article for qualitative comparison to the experimental data.

13

Supplementary Figure 13.
(**a**) Laser-induced magnetization dynamics (M/M_0) driven by circularly polarized fs NIR-pulses (1.55 eV) with opposite helicities ($\sigma_{\pm}$) for two different fluences 5 and 11 mJ/cm². The error bars are calculated as the standard error of the mean. (**b**) Maximum demagnetization amplitudes (D) measured upon $\sigma_{\pm}$-pumping and (**c**) their difference ΔM as a function of incident fluence. All values are normalized to the equilibrium magnetization in the unexcited state. The error bars of the D values correspond to the uncertainty of the fitted demagnetization amplitudes. The error bars of the ΔM values are calculated from the error propagation.

Energy (eV)	Wavelength (nm)	FEL seed (nm)	Pulse length (fs)
51.00$\pm$0.02	24.31$\pm$0.01	243.14 (10. harm.)	$\approx$92
54.10$\pm$0.02	22.92$\pm$0.01	251.90 (11. harm)	$\approx$89
56.10$\pm$0.02	22.10$\pm$0.01	243.14 (11. harm.)	$\approx$89
64.00$\pm$0.04	19.37$\pm$0.01	251.90 (13. harm.)	$\approx$84

Supplementary Table 1.
XUV photon energies and wavelengths used for excitation by tuning the FEL seeding laser wavelength and harmonics. The spectral bandwidth (energy resolution) is given by fitting the XUV spectrometer measurements with a Gaussian peak and taking the FWHM of the peak. The pulse lengths are approximated from the seeding laser pulse duration of $\approx$170 fs and its harmonic order[3].

14

Fluence (mJ/cm²)	B	τ_B (ps)	C	τ_C (ps)
1.3	0.165±0.006	0.006±0.116	-0.091±0.006	1.92±0.15
2.0	0.188±0.004	0.005±0.113	-0.094±0.004	2.67±0.15
2.7	0.283±0.004	0.160±0.011	-0.157±0.004	6.67±0.46
3.3	0.379±0.002	0.214±0.007	-0.223±0.005	13.8±0.8
4.0	0.428±0.006	0.171±0.018	-0.316±0.030	22.0±4.3
4.7	0.569±0.004	0.153±0.006	-0.339±0.025	21.9±3.0
5.3	0.691±0.002	0.206±0.003	-0.310±0.018	24.4±2.6
6.0	0.744±0.003	0.249±0.004	-0.280±0.014	18.6±2.0
6.7	0.793±0.003	0.241±0.003	-0.260±0.022	22.7±3.3
7.3	0.829±0.005	0.226±0.006	-0.328±0.323	50.0±61.2

Supplementary Table 2.
Fitted parameters of the transient magnetization dynamics upon σ₋-polarized excitation.

Fluence (mJ/cm²)	B	τ_B (ps)	C	τ_C (ps)
1.3	0.151±0.003	0.022±0.038	-0.067±0.003	2.25±0.18
2.0	0.231±0.005	0.054±0.017	-0.120±0.004	2.21±0.13
2.7	0.347±0.007	0.123±0.015	-0.170±0.007	3.35±0.24
3.3	0.463±0.004	0.130±0.007	-0.196±0.004	5.31±0.28
4.0	0.565±0.004	0.166±0.007	-0.212±0.005	8.35±0.61
4.7	0.593±0.008	0.141±0.012	-0.196±0.016	13.9±3.0
5.3	0.702±0.007	0.190±0.012	-0.196±0.022	16.7±4.3
6.0	0.792±0.005	0.193±0.007	-0.195±0.063	30.2±15.1
6.7	0.866±0.004	0.211±0.006	-0.175±0.179	50.0±67.2
7.3	0.928±0.004	0.226±0.005	-0.084±0.217	50.0±169.0

Supplementary Table 3.
Fitted parameters of the transient magnetization dynamics upon lin. hor. - polarized excitation.

Fluence (mJ/cm²)	B	τ_B (ps)	C	τ_C (ps)
1.3	0.166±0.004	0.072±0.018	-0.088±0.004	1.98±0.17
2.0	0.228±0.003	0.048±0.015	-0.119±0.003	2.25±0.09
2.7	0.363±0.007	0.215±0.015	-0.196±0.006	3.32±0.17
3.3	0.457±0.006	0.135±0.007	-0.975±4.653	50.0±253.0
4.0	0.676±0.008	0.276±0.011	-0.220±0.008	5.85±0.54
4.7	0.749±0.002	0.202±0.003	-0.191±0.077	50.0±26.5
5.3	0.813±0.005	0.201±0.005	-0.165±0.133	50.0±54.9
6.0	0.945±0.010	0.419±0.013	-0.639±0.295	50.0±31.5
6.7	0.959±0.004	0.276±0.005	-0.237±0.145	50.0±40.2
7.3	0.988±0.002	0.233±0.002	-0.096±0.066	50.0±44.9

Supplementary Table 4.
Fitted parameters of the transient magnetization dynamics upon σ₊-polarized excitation.

Fluence (mJ/cm²)	B	τ_B (ps)	C	τ_C (ps)
1.3	0.005±0.002	1.50±1.98	0	-
2.0	0.044±0.012	0.222±0.091	-0.033±0.012	1.64±0.66
2.7	0.097±0.103	0.529±0.338	-0.077±0.102	1.57±1.23
3.3	0.119±0.005	0.038±0.011	-0.098±0.016	2.82±1.08
4.0	0.202±0.004	0.328±0.028	0	-
4.7	0.174±0.008	0.355±0.029	0.153±0.008	9.37±1.86
5.3	0.115±0.005	0.150±0.020	0.140±0.007	8.78±1.67
6.0	0.202±0.005	1.18±0.09	0	-
6.7	0.136±0.009	0.334±0.043	0.114±0.009	4.84±0.94
7.3	0.141±0.006	0.222±0.025	0.119±0.023	11.9±5.4

Supplementary Table 5.
Fitted parameters of the difference between the transient magnetization dynamics upon σ₋- and σ₊-polarized excitation, i.e., of the helicity-dependent effect.

Supplementary References

1. Capotondi, F. *et al.* Multipurpose end-station for coherent diffraction imaging and scattering at FERMI@Elettra free-electron laser facility. *J. Synchrotron Radiat.* **22**, 544–552 (2015).
2. Cinquegrana, P. *et al.* The seed laser system of the FERMI free-electron laser: design, performance and near future upgrades. *High Power Laser Sci. Eng.* **9**, e61 (2021).
3. Finetti, P. *et al.* Pulse Duration of Seeded Free-Electron Lasers. *Phys Rev X* **7**, 021043 (2017).
4. Allaria, E. *et al.* Control of the Polarization of a Vacuum-Ultraviolet, High-Gain, Free-Electron Laser. *Phys Rev X* **4**, 041040 (2014).
5. Gutt, C. *et al.* Probing ultrafast changes of spin and charge density profiles with resonant XUV magnetic reflectivity at the free-electron laser FERMI. *Struct. Dyn.* **4**, 055101 (2017).
6. Ziolek, M. *et al.* The influence of the excitation geometry on the temporal resolution in femtosecond pump–probe experiments. *Opt. Commun.* **197**, 467–473 (2001).
7. Vijayakumar, M. & Gopinathan, M. S. Spin-orbit coupling constants of transition metal atoms and ions in density functional theory. *J. Mol. Struct. THEOCHEM* **361**, 15–19 (1996).
8. Willems, F. *et al.* Magneto-Optical Functions at the 3p Resonances of Fe, Co, and Ni: Ab initio Description and Experiment. *Phys Rev Lett* **122**, 217202 (2019).